

PAPER • OPEN ACCESS

How does the presence of neural probes affect extracellular potentials?

Recent citations

- [Espen Hagen et al](#)

To cite this article: Alessio Paolo Buccino *et al* 2019 *J. Neural Eng.* **16** 026030

View the [article online](#) for updates and enhancements.



The Department of Bioengineering at the University of Pittsburgh Swanson School of Engineering invites applications from accomplished individuals with a PhD or equivalent degree in bioengineering, biomedical engineering, or closely related disciplines for an open-rank, tenured/tenure-stream faculty position. We wish to recruit an individual with strong research accomplishments in Translational Bioengineering (i.e., leveraging basic science and engineering knowledge to develop innovative, translatable solutions impacting clinical practice and healthcare), with preference given to research focus on neuro-technologies, imaging, cardiovascular devices, and biomimetic and biorobotic design. It is expected that this individual will complement our current strengths in biomechanics, bioimaging, molecular, cellular, and systems engineering, medical product engineering, neural engineering, and tissue engineering and regenerative medicine. In addition, candidates must be committed to contributing to high quality education of a diverse student body at both the undergraduate and graduate levels.

[CLICK HERE FOR FURTHER DETAILS](#)

To ensure full consideration, applications must be received by June 30, 2019. However, applications will be reviewed as they are received. Early submission is highly encouraged.

How does the presence of neural probes affect extracellular potentials?

Alessio Paolo Buccino^{1,2}, Miroslav Kuchta³, Karoline Horgmo Jæger⁴,
Torbjørn Veffestad Ness^{1,5}, Pierre Berthet¹, Kent-Andre Mardal^{3,4},
Gert Cauwenberghs² and Aslak Tveito⁴

¹ Center for Integrative Neuroplasticity (CINPLA), Faculty of Mathematics and Natural Sciences, University of Oslo, Oslo, Norway

² Department of Bioengineering, University of California San Diego, San Diego, CA, United States of America

³ Department of Mathematics, University of Oslo, Oslo, Norway

⁴ Simula Research Laboratory, Oslo, Norway

⁵ Faculty of Science and Technology, Norwegian University of Life Sciences, Ås, Norway

E-mail: alessiob@ifi.uio.no

Received 27 March 2018, revised 24 January 2019

Accepted for publication 31 January 2019

Published 26 February 2019



Abstract

Objective. Mechanistic modeling of neurons is an essential component of computational neuroscience that enables scientists to simulate, explain, and explore neural activity. The conventional approach to simulation of extracellular neural recordings first computes transmembrane currents using the cable equation and then sums their contribution to model the extracellular potential. This two-step approach relies on the assumption that the extracellular space is an infinite and homogeneous conductive medium, while measurements are performed using neural probes. The main purpose of this paper is to assess to what extent the presence of the neural probes of varying shape and size impacts the extracellular field and how to correct for them. *Approach.* We apply a detailed modeling framework allowing explicit representation of the neuron and the probe to study the effect of the probes and thereby estimate the effect of ignoring it. We use meshes with simplified neurons and different types of probe and compare the extracellular action potentials with and without the probe in the extracellular space. We then compare various solutions to account for the probes' presence and introduce an efficient probe correction method to include the *probe effect* in modeling of extracellular potentials. *Main results.* Our computations show that microwires hardly influence the extracellular electric field and their effect can therefore be ignored. In contrast, multi-electrode arrays (MEAs) significantly affect the extracellular field by magnifying the recorded potential. While MEAs behave similarly to infinite insulated planes, we find that their effect strongly depends on the neuron-probe alignment and probe orientation. *Significance.* Ignoring the *probe effect* might be deleterious in some applications, such as neural localization and parameterization of neural models from extracellular recordings. Moreover, the presence of the probe can improve the interpretation of extracellular recordings, by providing a more accurate estimation of the extracellular potential generated by neuronal models.



Original content from this work may be used under the terms of the [Creative Commons Attribution 3.0 licence](https://creativecommons.org/licenses/by/3.0/). Any further distribution of this work must maintain attribution to the author(s) and the title of the work, journal citation and DOI.

Keywords: neural simulation, extracellular action potential, neural probes effect, finite element modeling, EMI model

(Some figures may appear in colour only in the online journal)

1. Introduction

Huge efforts have been invested in computational modeling of neurophysiology over the last decades. This has led to the development and public distribution of a large array of realistic neuron models, for example from the Blue Brain Project (bbp.epfl.ch [1, 2]), the Allen-Brain Institute brain cell database (celltypes.brain-map.org [3]), and the Neuromorpho database (neuromorpho.org [4, 5]). As experimental data become available, these models become both more elaborate and more accurate. However, some of the assumptions underlying the most commonly used models may not allow the accuracy necessary to obtain good agreements between models and experiments. For instance, it was pointed out in Tveito *et al* [6] that assumptions underlying the classical cable equation and the associated method for computing the extracellular potential, lead to significant errors both in the membrane potential and the extracellular potential. In the present paper we investigate whether the classical modeling techniques used in computational neurophysiology are sufficiently accurate to reflect measurements obtained by different types of probes, such as microwires/tetrodes, and larger silicon multi-electrode arrays (MEAs). Traditionally, these devices are not represented in the models describing the extracellular field, and our aim is to see if this omission introduces significant errors and how this mismatch could be accounted for in modeling of extracellular activity.

The most widely accepted and used modeling framework for computing the electrophysiology of neurons is the *cable equation* [7–12], which is used to find current and membrane potentials at different segments of a neuron. One straightforward and computationally convenient way to model the extracellular electric potential generated by neural activity is to sum the individual contributions of the transmembrane currents (computed for each segment) considering them as point current sources or line current sources [7, 11] using volume conductor theory. Although this approach represents the gold standard in computational neuroscience, there are some essential assumptions that need to be discussed. First, (i) the neuron is represented as a cable of discrete nodes and the continuous nature of its membrane is not preserved. Second, (ii) when solving the cable equation, the extracellular potential is neglected, but the extracellular potential is computed *a posteriori*. Third, and foremost, (iii) when computing extracellular potentials, the tissue in which the neuron lies is modeled as an infinite medium with homogeneous properties. The validity of these assumptions must be addressed in light of the specific application under consideration. The first assumption (i) can be justified by increasing the number of nodes in the model, but assumption (ii) is harder to relax since it means that the

model ignores ephaptic effects. Therefore, this assumption has gained considerable attention [6, 13–18]. However, the main focus of the present paper is assumption (iii). More specifically our aim is to study the effect of the physical presence of a neural probe on the extracellular signals. Can it be neglected in the mathematical model, or should it be included as a restriction on the extracellular domain? Specifically, is the conventional modeling framework, ignoring the effect of the probes, sufficient to yield reliable prediction of extracellular potentials? Finally, what can modelers do in order to represent and include the effect of recording probes?

In order to investigate this question, we have used the extracellular-membrane-intracellular (EMI) model [6, 19, 20]. The EMI model allows for explicit representation of both the intracellular space of the neuron, the cell membrane and the extracellular space surrounding the neuron. Therefore, the geometry of neural probes can be represented accurately in the model. We have run finite element simulations of simplified pyramidal cells combined with different types of probes, such as microwires/tetrodes, and larger silicon multi-electrode arrays (MEAs).

Our computations strongly indicate that the effect of the probe depends on several factors; small probes (microwires) have little effect on the extracellular potential, whereas larger devices (such as multi-electrode arrays, MEAs) change the extracellular potential quite dramatically, resembling the effect of a non-conductive infinite plane in the proximity of the neuron. The effect, however, depends on the neuron-probe alignment and orientation. We then compare the EMI results with conventional cable equation-based techniques, such as the current summation approach [11, 20], the hybrid solution [20–23], and the method of images [24, 25] and introduce the probe correction method, which allows to reach a hybrid solution accuracy leveraging on a pre-mapping of the probe-specific effect and the reciprocity principle.

The results may aid in understanding experimental data recorded with MEAs, it may improve accuracy when extracellular potentials are used to parameterize membrane models as advocated in [26], and to localize and classify neurons from MEA recordings [27, 28].

The rest of the article is organized as follows: in section 2 we describe the methods used throughout the paper, with particular focus on the EMI model (section 2.1), the meshes (section 2.2), the finite element framework (section 2.3), and modeling approaches used for comparison (section 2.4). In section 3 we present our findings related to the effect of probes of different geometry on the extracellular recordings (section 3.1), the variability of our simulations depending on geometrical parameters of the mesh (section 3.2), before comparing them with results obtained from other computational

approaches (section 3.3) and the relative computational costs of these methods (section 3.4). Finally, we discuss and contextualize the work in section 4.

2. Methods

In this section we introduce the modeling frameworks used to investigate the effect of the probes on the extracellular potential. In particular we first describe the EMI model, the meshes, and the membrane and finite element modeling. Then, we describe the conventional modeling based on the cable equation solution: the current summation approach (CS), the hybrid solution (HS) and the method of images (MoI). Finally, we introduce the probe correction method (PC), which reaches the hybrid solution accuracy in a more efficient and computationally-cheap way.

2.1. The extracellular-membrane-intracellular model

The purpose of the present report is to estimate the effect of introducing a probe in the extracellular domain on the extracellular potential. This can be done using a model discussed in [6, 19, 29–31] referred to as the EMI model. In the EMI model the extracellular space surrounding the neuron, the membrane of the neuron and the intracellular space of the neuron are all explicitly represented in the model. The model takes the form

$$\nabla \cdot \sigma_i \nabla u_i = 0 \quad \text{in } \Omega_i, \quad (1)$$

$$\nabla \cdot \sigma_e \nabla u_e = 0 \quad \text{in } \Omega_e, \quad (2)$$

$$u_e = 0 \quad \text{at } \partial\Omega_e, \quad (3)$$

$$\sigma_e \nabla u_e \cdot n_e = 0 \quad \text{at } \partial\Omega_p, \quad (4)$$

$$n_e \cdot \sigma_e \nabla u_e = -n_i \cdot \sigma_i \nabla u_i \stackrel{\text{def}}{=} I_m \quad \text{at } \Gamma, \quad (5)$$

$$u_i - u_e = v \quad \text{at } \Gamma, \quad (6)$$

$$\frac{\partial v}{\partial t} = \frac{1}{C_m} (I_m - I_{\text{ion}}) \quad \text{at } \Gamma. \quad (7)$$

In the simplified geometry sketched in figure 1, Ω denotes the total computational domain consisting of the extracellular domain Ω_e and the intracellular domain Ω_i , and the cell membrane is denoted by Γ . n_i and n_e are the vectors normal to Γ pointing out of the intra- and extracellular domains, respectively. u_i and u_e denote the intra- and extracellular potentials, and $v = u_i - u_e$ denotes the membrane potential defined at the membrane Γ . The intra- and extracellular conductivities are given respectively by σ_i and σ_e and in this work we assume that the quantities are constant scalars. The cell membrane capacitance is given by C_m , and the ion current density is given by I_{ion} . I_m is the total current current escaping through the membrane.

The EMI model is here considered with grounding (Dirichlet) boundary conditions, i.e. $u_e = 0$, on the boundary of the extracellular domain ($\partial\Omega_e$) while insulating (Neumann)

boundary conditions, i.e. $\sigma_e \nabla u_e \cdot n_e = 0$, were prescribed at the surface of the probe ($\partial\Omega_p$). Note that the latter is a suitable boundary condition also for the conducting surfaces of the probe [25, 32]. The resting potential (see table 1) is used as initial condition for v .

2.2. Meshes

In order to implement the EMI model described above, the computational domain was discretized by unstructured tetrahedral meshes generated by `gmsh` [33]. We used a simplified neuron model similar to a ball-and-stick model [34, 35], with a spherical soma with 20 μm diameter—whose center is in the origin of the axis—an apical dendrite of length $L_d = 400 \mu\text{m}$ and diameter $D_d = 5 \mu\text{m}$ in the positive z direction and an axon of length $L_d = 200 \mu\text{m}$ and diameter $D_d = 2 \mu\text{m}$ in the negative z direction. Both the axon and the dendrites are connected to the soma via a tapering in the geometry. On the dendritic side, the diameter at the soma is 8 μm and it linearly reduces to 5 μm in a 20 μm portion. On the axonal side, the *axon hillock* has a diameter of 4 μm at the soma and it is tapered to 2 μm in 10 μm .

The neuron was placed in a box with and without neural probes to study the effect of the recording device on the simulated signals. We used three different types of probes:

Microwire: the first type of probe represents a microwire type of probe (or tetrode). For this kind of probes we used a cylindrical insulated model with 30 μm diameter. The extracellular potential, after the simulations, was estimated as the average of the electric potential measured at the tip of the cylinder. The microwire probe is shown in figure 2(A) alongside with the simplified neuron.

Neuronexus (MEA): the second type of probe model represents a commercially available silicon MEA (A1x32-Poly3-5mm-25s-177-CM32 probe from Neuronexus Technologies), which has 32 electrodes in three columns (the central column has 12 recording sites and first and third columns have 10) with hexagonal arrangement, a y -pitch of 18 μm , and a z -pitch of 22 μm . The electrode radius is 7.5 μm . This probe has a thickness of 15 μm and a maximum width of 114 μm , and it is shown in figure 2(B).

Neuropixels (MEA): the third type of probe model represents the Neuropixels silicon MEA [36]. The original probe has more than 900 electrodes over a 1 cm shank, it is 70 μm wide and 20 μm thick. In our mesh, shown in figure 2(C) we used 24 $12 \times 12 \mu\text{m}$ recording sites arranged in the *chessboard* configuration with an inter-electrode-distance of 25 μm [36].

In order to evaluate the effect of the described probes depending on the relative distance to the neuron (x direction), we generated several meshes in which the distance between the contact sites and the center of the neuron was 17.5, 22.5, 27.5, 37.5, 47.5, and 77.5 μm . Note that these distances refer to the beginning of the microwire tip (which extends in the x direction for 30 μm) and to the MEA $y - z$ plane (for the MEA

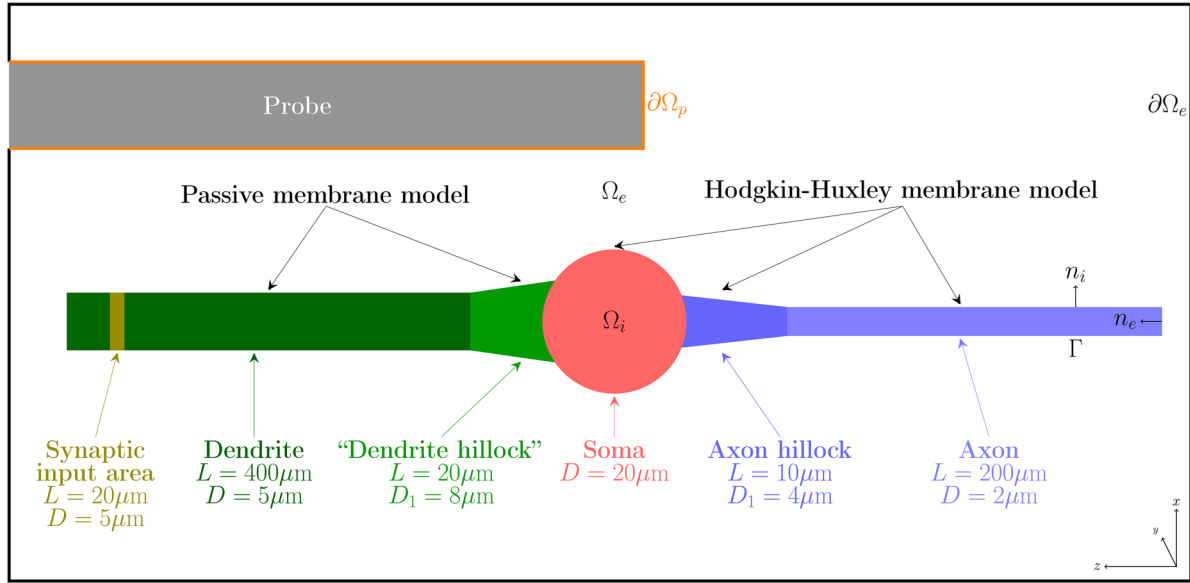


Figure 1. Sketch of the simplified neuron geometry and its surroundings. The intracellular domain is denoted by Ω_i , the cell membrane is denoted by Γ , and the extracellular domain is denoted by Ω_e . The boundary of the probe is denoted by $\partial\Omega_p$ and the remaining boundary of the extracellular domain is denoted by $\partial\Omega_e$. The normal vector pointing out of Ω_i is denoted by n_i , and n_e denotes the normal vector pointing out of Ω_e . L and D are the length and diameter of neural segments, respectively, and D_1 is the diameter of the *hillocks* in correspondence of the soma. In our simulations, we consider three types of probe geometry (see figure 2). Note that the probe interior is *not* part of the computational domain.

probes the recording sites do not extend in the x direction). When not specified, instead, the distance for the microwire probe was $25 \mu\text{m}$, $32.5 \mu\text{m}$ for the Neuronexus MEA probe, and $30 \mu\text{m}$ for the Neuropixels probe (center of the probe tip at $40 \mu\text{m}$).

To investigate if and how the bounding box size affects the simulation, since the electric potential is set to zero at its surface, we generated meshes with five different box sizes. Defining dx , dy , and dz as the distance between the extremity of the neuron and the box in the x , y , and z directions, the three box sizes were:

- size 1:** $dx = 80 \mu\text{m}$, $dy = 80 \mu\text{m}$, and $dz = 20 \mu\text{m}$
- size 2:** $dx = 100 \mu\text{m}$, $dy = 100 \mu\text{m}$, and $dz = 40 \mu\text{m}$
- size 3:** $dx = 120 \mu\text{m}$, $dy = 120 \mu\text{m}$, and $dz = 60 \mu\text{m}$
- size 4:** $dx = 160 \mu\text{m}$, $dy = 160 \mu\text{m}$, and $dz = 100 \mu\text{m}$
- size 5:** $dx = 200 \mu\text{m}$, $dy = 200 \mu\text{m}$, and $dz = 150 \mu\text{m}$

Moreover, we evaluated the solution convergence depending on the resolution by generating meshes with four different resolutions. Defining r_n , r_p , and r_{ext} as the resolutions/typical mesh element sizes for the neuron volume and membrane, for the probe, and for the bounding box surface, respectively, the four degrees of *coarseness* were:

- coarse 0:** $r_n = 2 \mu\text{m}$, $r_p = 5 \mu\text{m}$, and $r_{ext} = 7.5 \mu\text{m}$
- coarse 1:** $r_n = 3 \mu\text{m}$, $r_p = 6 \mu\text{m}$, and $r_{ext} = 9 \mu\text{m}$
- coarse 2:** $r_n = 4 \mu\text{m}$, $r_p = 8 \mu\text{m}$, and $r_{ext} = 12 \mu\text{m}$
- coarse 3:** $r_n = 4 \mu\text{m}$, $r_p = 10 \mu\text{m}$, and $r_{ext} = 15 \mu\text{m}$

At the interface between two resolutions, the mesh size was determined as their minimum. Further, having instructed gmsh to not allow hanging nodes the mesh in the surroundings of the neuron and probe is gradually coarsened to r_{ext} resolution.

Table 1. Model parameters used in the simulations. The parameters of the Hodgkin–Huxley model are given in [37].

Parameter	Value	Parameter	Value
C_m	$1 \mu\text{F cm}^{-2}$	g_{syn}	10 mS cm^{-2}
σ_i	7 mS cm^{-1}	v_{eq}	0 mV
σ_e	3 mS cm^{-1}	t_0	0.01 ms
g_L	0.06 mS cm^{-2}	α	2 ms
v_{rest}	-75 mV		

For each of the mesh configuration with varying probe model, box size, and coarseness we simulated the extracellular signals with and without the probe in the extracellular space and sampled the electric potential at the recording site locations (even when the probe is absent).

2.3. Membrane model and finite element implementation

On the membrane of the soma and the axon, the ionic current density, I_{ion} , is computed by the Hodgkin–Huxley model with standard parameters as given in [37]. On the membrane of the dendrite, we apply a passive membrane model with a synaptic input current of the form

$$I_{\text{ion}} = I_{\text{leak}} + I_{\text{syn}}, \quad (8)$$

$$I_{\text{leak}} = g_L(v - v_{\text{rest}}), \quad (9)$$

$$I_{\text{syn}} = g_s(\mathbf{x})e^{-\frac{t-t_0}{\alpha}}(v - v_{\text{eq}}), \quad (10)$$

where

$$g_s(\mathbf{x}) = \begin{cases} g_{\text{syn}}, & \text{for } \mathbf{x} \text{ in the synaptic input area,} \\ 0, & \text{elsewhere.} \end{cases} \quad (11)$$

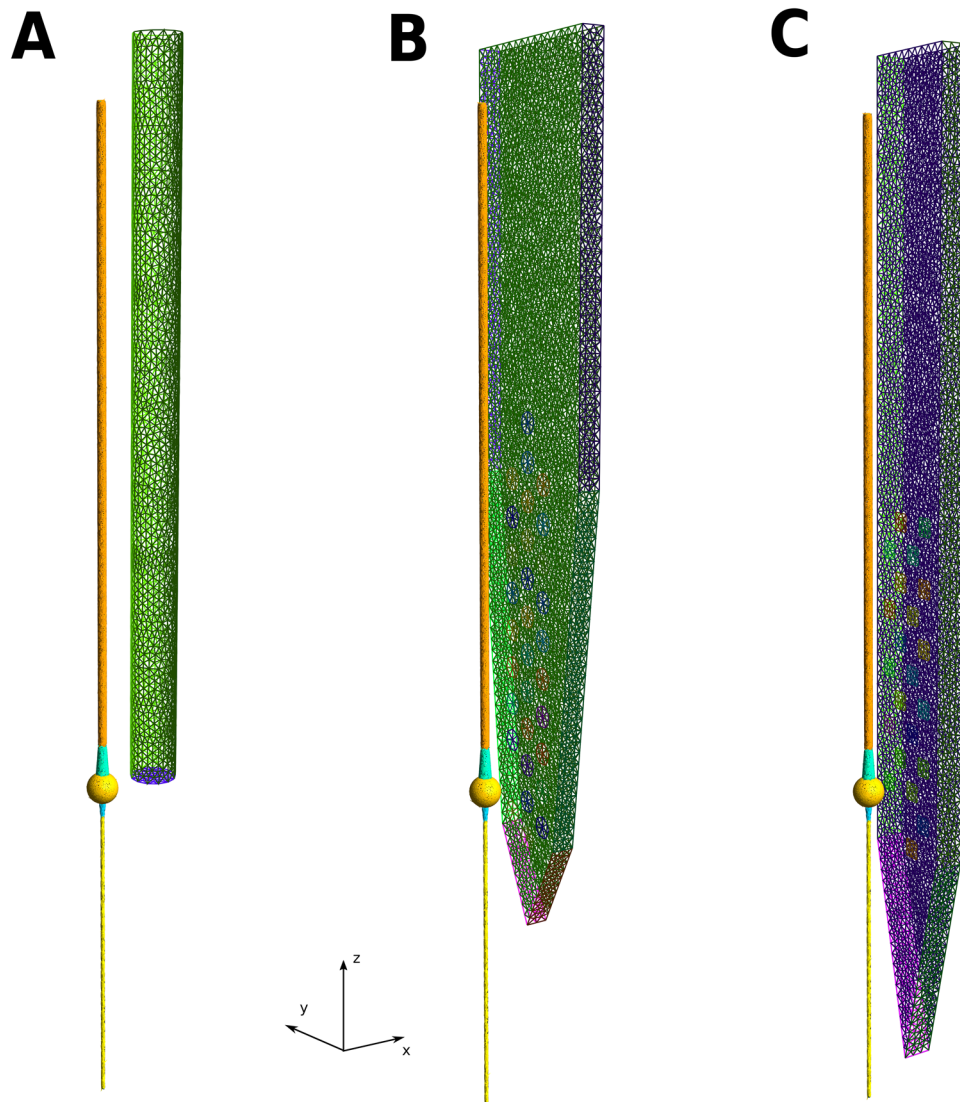


Figure 2. Visualization of simplified neuron and probe meshes. (A) Microwire: the probe has a $15\ \mu\text{m}$ radius and it is aligned to the neuronal axis (z direction) and the center of the probe tip is at $(40, 0, 0)\ \mu\text{m}$ (the soma center is at $(0, 0, 0)\ \mu\text{m}$). The axon and soma of the neuron are depicted in yellow, the dendrite is orange, and the axon and *dendritic* hillock are in cyan. (B) Neuronex MEA: the probe represents a Neuronex A1x32-Poly3-5mm-25s-177-CM32 with recording sites facing the neuron. The MEA is $15\ \mu\text{m}$ thick and the center of the bottom vertex is at $(40, 0, -100)\ \mu\text{m}$. The maximum width of the probe is $114\ \mu\text{m}$, which makes it almost four times larger than the microwire probe. (C) Neuropixels MEA: this probe [36] has a width of $70\ \mu\text{m}$, a thickness of $20\ \mu\text{m}$, and the center of the bottom vertex is at $(40, 0, -100)\ \mu\text{m}$. All meshes represented here are built with the finest coarseness described in the text (*coarse 0*).

The parameters of the dendrite model are given in table 1, and the synaptic input area is defined as a section of the dendrite of length $20\ \mu\text{m}$ located $350\ \mu\text{m}$ from the soma, as illustrated in figure 1.

The EMI model (1)–(7) is solved by the operator splitting scheme and the $H(\text{div})$ discretization proposed in [20]. In this scheme a single step of the EMI model consists of two sub-steps. First, assuming the current membrane potential v is known, the ordinary differential equations (ODE) of the membrane model are solved yielding a new membrane state and the value of v . Next, equation (7), discretized in time with I_{ion} set to zero, is solved together with equations (1)–(6) using the computed value of v as input. This step yields the new values of intra/extra-cellular potentials u_i , u_e and the transmembrane potential v . The $H(\text{div})$ approach then means that the EMI model is transformed by introducing unknown electrical fields

$\sigma_i \nabla u_i$ and $\sigma_e \nabla u_e$ in addition to the potentials u_i , u_e and v . Thus more unknowns are involved, however, the formulation leads to more accurate solutions, see [20, section 3].

In our implementation the ODE solver for the first step of the operator splitting scheme is implemented on top of the computational cardiac electrophysiology framework `cbc.beat` [38]. For the second step, the $H(\text{div})$ formulation of the EMI model, see [20, section 2.3.3], is discretized by the finite element method (FEM) using the `FEniCS` library [39]. More specifically, the electrical fields are discretized by the lowest order Raviart–Thomas elements [40] while the potentials use piecewise constant elements. The linear system due to implicit/backward-Euler temporal discretization in equation (7) and FEM is finally solved with the direct solver `MUMPS` [41] which is interfaced with `FEniCS` via the `PETSc` [42] linear algebra library.

2.4. Other modeling approaches

2.4.1. Current summation (CS), method of images (MoI), and scaled current summation (SCS). The cable equation [43–45] is of great importance in computational neuroscience, and it reads,

$$C_m \frac{\partial v}{\partial t} + I_{\text{ion}} = \eta \frac{\partial^2 v}{\partial x^2}, \quad (12)$$

where v is the membrane potential of the neuron, C_m is the membrane capacitance, I_{ion} is the ion current density and $\eta = \frac{h\sigma_i}{4}$, where h is the diameter of the neuron, and σ_i denotes the intracellular conductivity of the neuron [43].

This equation is used to compute the membrane potential of a neuron and the solution is commonly obtained by dividing the neuron into compartments and replacing the continuous model (12) by a discrete model [43]. In order to compute the associated extracellular potential, it is common to use the solution of the cable equation to compute the transmembrane currents densities in every compartment, and then invoke the classical summation formula,

$$u_e(x, y, z) = \frac{1}{4\pi\sigma_e} \sum_k \frac{I_k}{|\mathbf{r} - \mathbf{r}_k|}. \quad (13)$$

Here, σ_e is the constant extracellular conductivity (in all the implemented models, the milieu is assumed to be linear by using a constant σ_e), \mathbf{r}_k is the center of the k th compartment of the neuron, $|\mathbf{r} - \mathbf{r}_k|$ denotes the Euclidean distance from $\mathbf{r} = \mathbf{r}(x, y, z)$ to the point \mathbf{r}_k , and I_k denotes the transmembrane current of each compartment. This solution assumes that the extracellular milieu is purely conductive, infinite, and homogeneous. We denote this method as current summation approach (CS) [6].

As the silicon probes are made of insulated material, they could be approximated with the method of images (MoI) [12, 24, 25]. With the MoI the probe is assumed to be an infinite insulating plane, effectively increasing the extracellular potential by a factor of 2. Using the MoI, the factor 2 can be explained as follows: for each current source, an *image* current source is introduced in the mirror position with respect to the insulating plane, effectively doubling the potential in proximity of the plane and canceling current densities normal to the plane. For the MoI, the summation formula (equation 13) reads:

$$u_e(x, y, z) = \frac{1}{2\pi\sigma_e} \sum_k \frac{I_k}{|\mathbf{r} - \mathbf{r}_k|}. \quad (14)$$

As will be shown section 3.1, the peak scaling factor (1 and 2 for the CS and MoI solutions, respectively) of the modeled probes is modulated by the neuron-probe alignment, rotation, and by the probe type and it can be a value between 0 and 2 depending on these factors. Therefore, we also propose and compare a third current summation-based approach, namely scaled current summation (SCS), in which the scale factor is set to match the peak ratio between the hybrid solution (section 2.4.2) and the CS solution on the electrode with largest amplitude (e.g. 1.65 is used in section 3.3.1).

We implemented the same simulations presented in section 2.1 using the conventional modeling approach described above (CS) to compare them with the EMI simulations. We used LFPY [11, 12], running upon NEURON 7.5 [9, 10], to solve the cable equation and compute extracellular potentials using equation (13). As morphology, we used a ball-and-stick model with an axon with the same geometrical properties described in section 2.2. Similarly to the EMI simulations, we used a synaptic input in the middle of the dendritic region activated in the EMI simulation ($z = 360 \mu\text{m}$) to induce a single spike and we observed the extracellular potentials on the recording sites. The synaptic weight was adjusted so that the extracellular largest peak was coincident in time with the one from the EMI simulation. To model the spatial extent of the electrodes, we randomly drew 50 points within a recording site and we averaged the extracellular potential computed at these points [11]. We used the same parameters shown in table 1 (note that in NEURON conductances are defined in S cm^{-2} so we set $g_L = g_{\text{pas}} = 0.06 \cdot 10^{-3} \text{ S cm}^{-2}$) and we used an axial resistance R_a of $150 \Omega \text{ cm}^{-1}$. The `fixed_length` method was used as discretization method with a fixed length of $1 \mu\text{m}$, yielding 658 segments (23 somatic, 422 dendritic, and 213 axonal). Transmembrane currents were considered as current point sources in their contributions to the extracellular potential, following equation (13) (using LFPY `point-source` argument of the `RecExtElectrode` class). The MoI and SCS solutions were calculated by multiplying the CS solution by a factor 2 and 1.65 (optimized scale factor using the hybrid solution).

2.4.2. Hybrid solution (HS). The hybrid solution (HS) [21–23] combines the transmembrane currents for each neural segments computed with the cable equation and a finite element modeling for the extracellular space. The transmembrane currents are used as source terms in a finite element solution of the Poisson Equation in the extracellular space (equation (2)), using an iterative solver for the Poisson problem, specifically, preconditioned conjugate gradients with algebraic multigrid preconditioning). With this approach, the probe can be explicitly modeled using insulating (Neumann) boundary conditions at the surface of the probe (equation (5)) and the differences between the HS and the EMI solution lie in differences regarding the modeling of the neuron dynamics, such as the self-ephaptic effect. The HS requires that a FEM simulation is run for each timestep of the transmembrane currents, each time setting the source terms with the currents at the specific timestep. This makes it computationally expensive, especially, for long simulations. Alternatively, one could run a single FEM simulation for each neural segment with a unitary test current and then use the potentials computed at the recording sites as a static map for summing the contribution of all currents at each timestep. The latter approach can be also computationally complex, as the number of segments in the multi-compartment simulation can be quite high and it would require to store in memory a large number of finite element solutions.

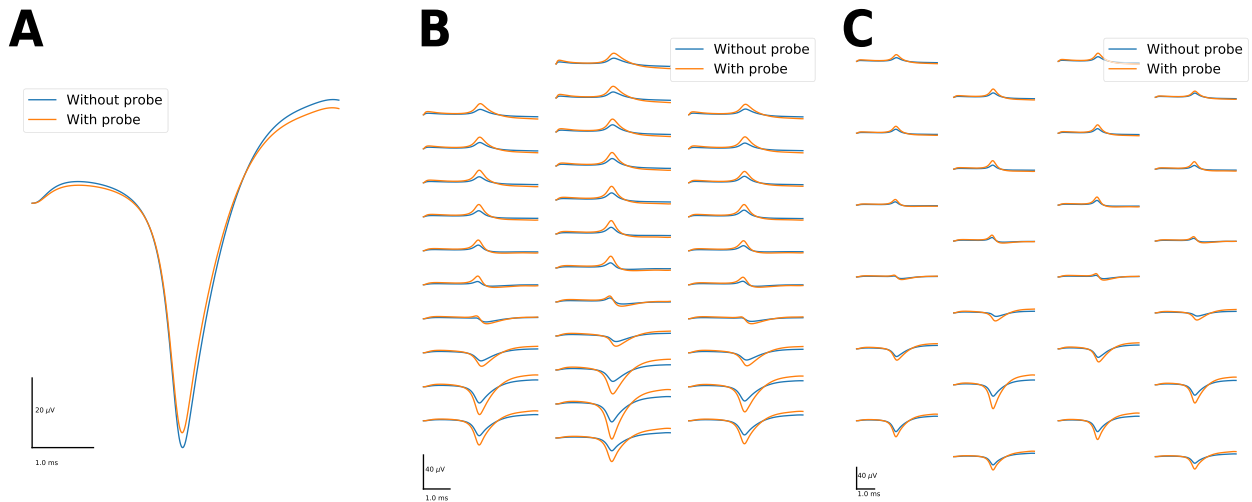


Figure 3. Extracellular action potentials (EAPs). (A) EAPs without (blue) and with (orange) the microwire probe (single recording site) in the extracellular space. The amplitude difference in the largest peak is only $1.03 \mu\text{V}$, which is negligible for most applications. (B) Same as (A) but with the Neuronexus MEA probe. For this probe, the difference in amplitude is $20.17 \mu\text{V}$ (the solution with the MEA is almost twice as large as the one without the MEA in the extracellular space). (C) Same as (A) but with the Neuropixels MEA probe. For this probe, the difference in amplitude is $23.16 \mu\text{V}$.

2.4.3. Probe correction (PC). The hybrid solution is a good and widely used approach to model a non-homogeneous extracellular space, especially in the peripheral nervous system literature [21–23]. However, it requires to run a finite element simulation for every neuron simulation, as transmembrane currents are located in different positions for different neurons.

In order to overcome this issue, we designed the probe correction method (PC) that relies on the reciprocity principle [46] and the principle of superimposition (given the assumption of linearity of the milieu expressed in section 2.4.1). The reciprocity principle states that if a current I_1 in a position (x_1, y_1, z_1) generates a potential u_1 in a second position (x_2, y_2, z_2) , then the same current I_1 placed in (x_2, y_2, z_2) will result in a potential u_1 in (x_1, y_1, z_1) ⁶. Using this principle, we first simulated with a finite element method the extracellular potential generated by a test current (1 nA) from each electrode i of a specific probe (e.g. Neuronexus) in any point of the extracellular space and define it as $u_i(x_i, y_i, z_i)$, where (x_i, y_i, z_i) is the relative position with respect to the electrode i . Also in this case we used an iterative solver for the Poisson problem (preconditioned conjugate gradients with algebraic multigrid preconditioning). Then, leveraging on the reciprocity and superimposition principles, we mapped the contribution of each transmembrane current to the potential at each electrode i as: $u_{ik} = I_k u_i(x_k, y_k, z_k)$, where (x_k, y_k, z_k) is now the relative position between the k th neural segment and the electrode i , and I_k is the transmembrane current for the k th neural segment. The potential at each electrode i can be computed as:

$$u_i = \sum_k u_{ik} = \sum_k I_k u_i(x_k, y_k, z_k).$$

The PC method allows to pre-compute the effect of a probe in the extracellular space and then use this mapping for any

⁶The reciprocity principle was originally derived for static charges and extended here to static currents.

neural model, without the need to run a full FEM simulation. The number of FEM solutions that need to be computed and stored during the pre-mapping is equal to the number of electrodes in the probe.

3. Results

In this section we present results of numerical simulations which quantify the effect of introducing probes in the extracellular domain on the extracellular potential. We show how this effect depends on the distance between the neuron and the probe, their lateral alignment, and the probe rotation. The evaluation of the *probe effect* (section 3.1) is carried out using the EMI simulation framework. Furthermore, we evaluate the numerical variability of the EMI solutions (section 3.2), we compare with other modeling schemes (section 3.3), and finally report CPU-efforts for the simulations (section 3.4).

3.1. The probe effect

3.1.1. The geometry of the probe affects the recorded signals. The first question that we investigated is whether the probes have an effect and, if so, how substantial this effect is and if it depends on the probe geometry. In order to do so we analyzed the extracellular action potential (EAP) traces with and without placing the probe in the mesh.

In figure 3 we show the EAP with and without the microwire probe (A), the Neuronexus probe (B), and the Neuropixels probe (C). The blue traces are the extracellular potentials computed at the recording sites when the probe was removed, while the orange traces show the potential when the probe is present in the extracellular space. In this case the probe tip was placed $40 \mu\text{m}$ from the soma center, we used a box of size 2 and coarse 2 resolution. It is clear that the *probe effect*

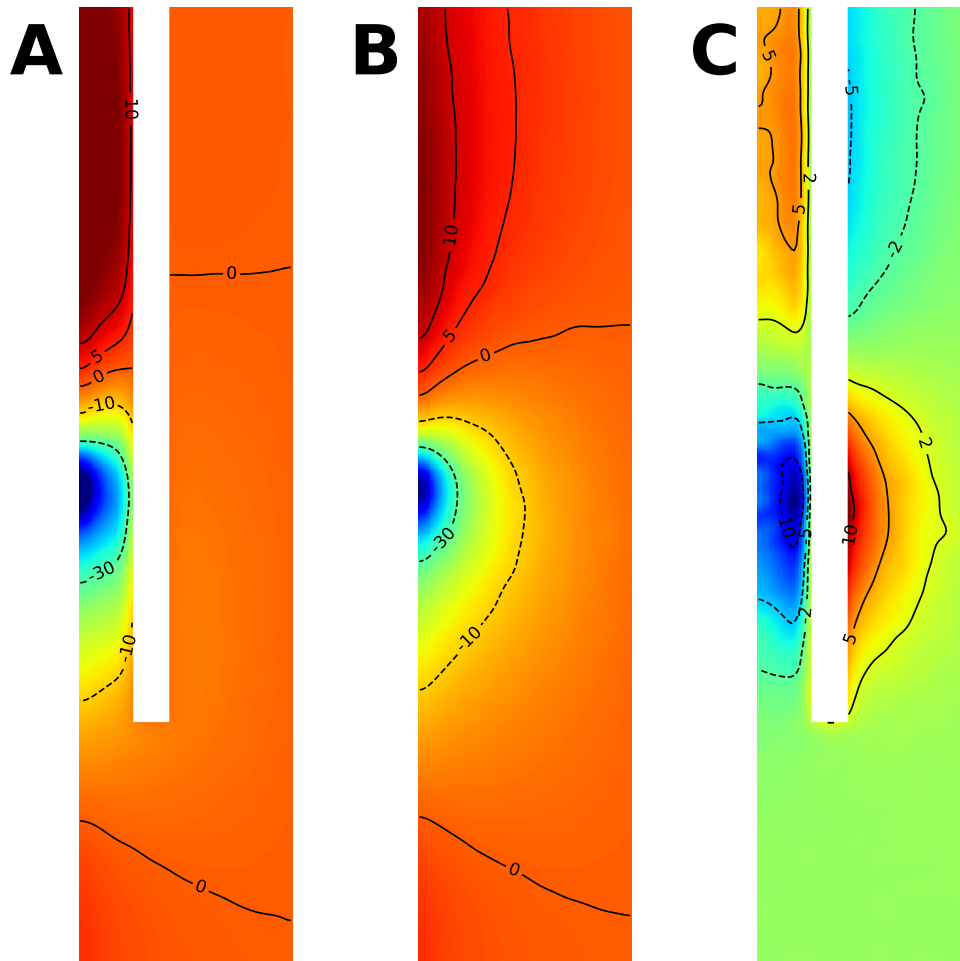


Figure 4. Extracellular potential distribution on the $x - z$ plane with the Neuronexus MEA probe (A) without the probe (B), and their difference (C). The images were smoothed with a gaussian filter with standard deviation of $4 \mu\text{m}$. The color code for panel A and B is the same. The isopotential lines show the potential in μV . The probe (white area) acts as an insulator, effectively increasing the extracellular potential (in absolute value) in the area between the neuron and the probe (panel C, blue colors close to the soma and red close to the dendrite) and decreasing it behind the probe of several μV . The effect is smaller at the tip of the probe (the green color represents a $0 \mu\text{V}$ difference).

is more prevalent for the MEA probes than for the microwire, suggesting that the physical size and geometry of the probe play an important role. In particular, for the Neuronexus probe the minimum peak without the probe is $-21.09 \mu\text{V}$ and with the probe it is $-41.26 \mu\text{V}$: the difference is $20.17 \mu\text{V}$. For the Neuropixels probe the peak with no probe is $-21.2 \mu\text{V}$, with the probe it is $-44.36 \mu\text{V}$ and the difference is $23.16 \mu\text{V}$. In case of the microwire type of probe, the effect is minimal: the minimum peak without the probe is $-16.85 \mu\text{V}$, with the probe it is $-15.82 \mu\text{V}$, and the difference is about $1.03 \mu\text{V}$ (the peak without the probe is even larger than the one with the probe). Note that the values for the microwire are slightly lower than the MEAs because even if the microwire tip center is at the same distance ($40 \mu\text{m}$), it extends for $30 \mu\text{m}$ in the x direction, effectively lowering the recorded potential due to the fast decay of the extracellular potential with distance. The recording sites of the MEAs, instead, lie on the $y - z$ plane, at a fixed distance.

The MEAs, electrically speaking, are like insulating walls that do not allow currents to flow in. The insulating effect can

be appreciated in figure 4, in which the extracellular potential at the time of the peak is computed in the $[10, 100] \mu\text{m}$ interval in the x direction and in the $[-200, 200] \mu\text{m}$ interval in the z direction (the origin is the center of the soma). Panel A shows the extracellular potential with the probe (Neuronexus) and panel B without the probe. The currents are deflected due to the presence of the probe, and this causes an increase (in absolute value) in the extracellular potential between the neuron and the probe, as shown in panel C, where the difference of the extracellular potential with and without probe is depicted. The substantial effect using the MEA probe probably also depends on the arrangement of the recording sites: while for the MEAs, the electrodes *face* the neuron (they lie on the $y - z$ plane) and currents emitted by the membrane cannot flow in the x direction due to the presence of the probe, for the microwire, the electrode is at the tip of the probe (at $z = 0$, extending in the $x - y$ plane—see figure 2) and currents can *naturally* flow downwards in the x direction, yielding a little effect (figure 4(C) shows that the effect at the tip of the MEA probe is almost null).

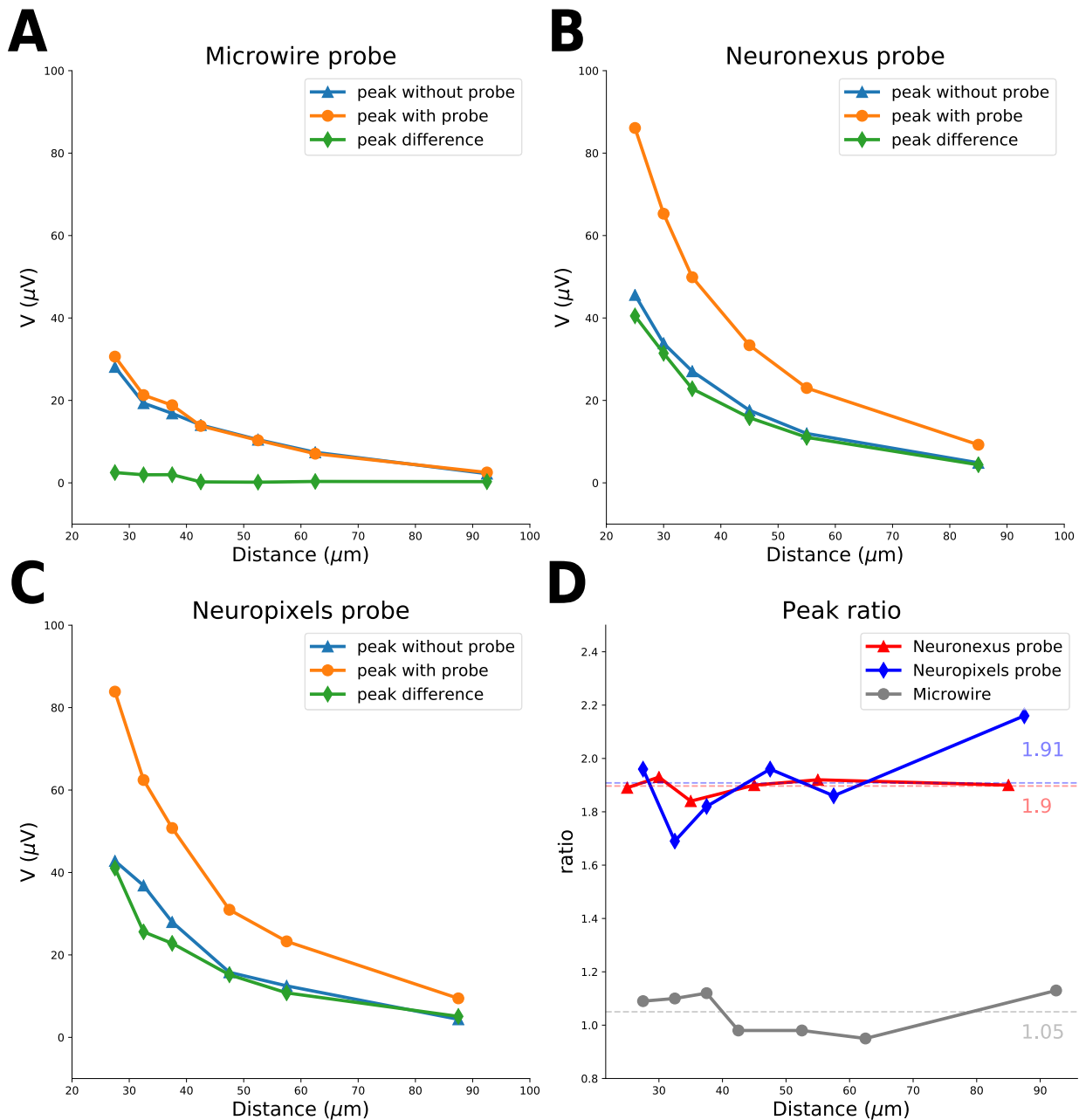


Figure 5. Differences in EAP maximum absolute value peak with and without probe depending on distance. (A) Microwire probe: maximum peak without probe (blue), with probe (orange), and their difference (green). The difference is small even when the probe is close to the neuron. (B) Neuronexus MEA probe: maximum peak without probe (blue), with probe (orange), and their difference (green). The difference is large at short distances and it decays at larger distances. (C) Neuropixels MEA probe: maximum peak without probe (blue), with probe (orange), and their difference (green). Also for this probe the difference is large at short distances and it reduces at further away from the neuron. (D) Ratio between peak with and without probe for the Neuronexus (red), the Neuropixels (blue) and the microwire probe (grey). The ratio is almost constant at different distances and the average value is 1.9 for the Neuronexus, 1.91 for the Neuropixels, and 1.05 for the microwire probe.

3.1.2. The amplitude ratio is constant with probe distance. In this section we analyze the trend of the probe-induced error depending on the vicinity of the probe. We swept the extracellular space from a closest distance between the probe and the somatic membrane of $7.5 \mu\text{m}$ to a maximum distance of $67.5 \mu\text{m}$.

In figures 5(A)–(C) we plot the absolute peak values with (orange) and without probe (blue), as well as their difference (green) for the microwire (A), Neuronexus (B) and

Neuropixels (C) probes. For the microwire (A), as observed in the previous section, the *probe effect* is small and the maximum difference is $1.97 \mu\text{V}$, which is 10.1% of the amplitude without probe, when the probe is closest. For the Neuronexus MEA probe (B), at short distances the difference between the peaks with and without probe is large— $40.5 \mu\text{V}$ (88.8% of the amplitude without probe) at $7.5 \mu\text{m}$ probe-membrane distance—and it decreases as the probe distance increases. At the farthest distance, where the probe tip is at $75 \mu\text{m}$ from the

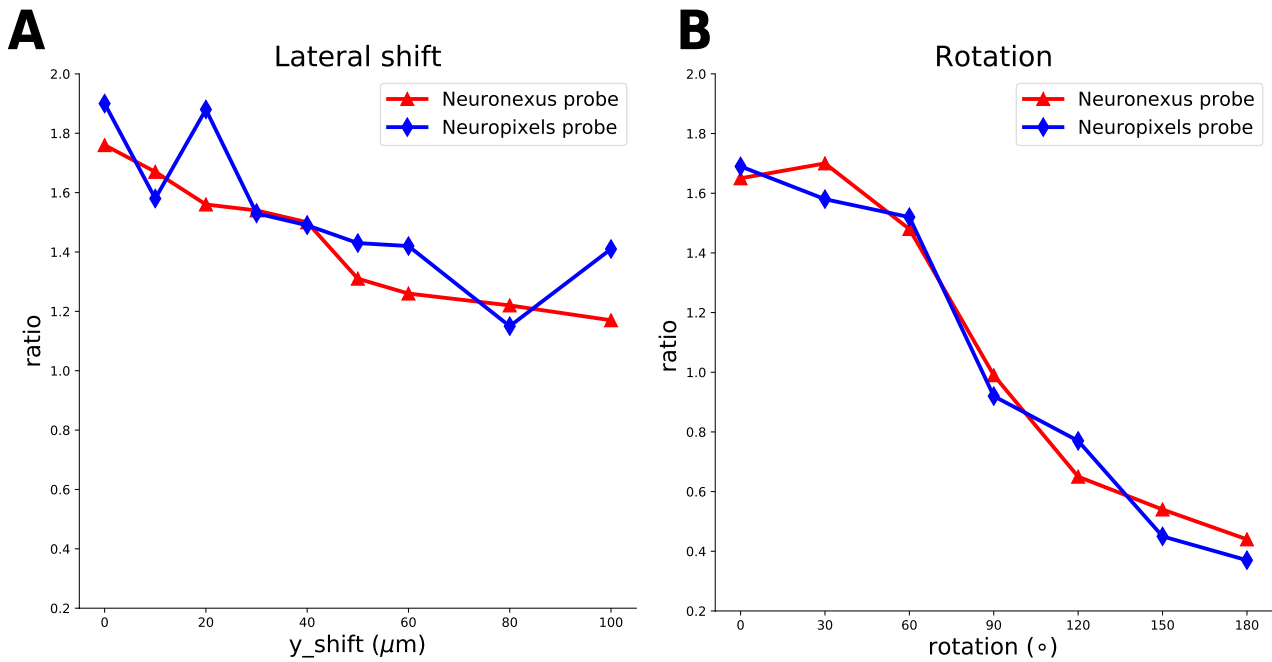


Figure 6. Effects of neuron probe alignment. (A) Amplitude ratio for different y lateral shifts for the Neuronexus (red) and Neuropixels (blue) probes. The ratio decreases almost linearly with the y shift. (B) Amplitude ratio for different probe rotations for the Neuronexus (red) and Neuropixels (blue) probes. At small rotations, the peak ratio is between 1.6 and 1.8, at 90° rotation (when the probe exposes its thinnest side to the neuron) it is around 1, and between 90° and 180° the shadowing effect of the probe makes the ratio lower than 1.

somatic membrane, the difference is $4.38 \mu\text{V}$, which is 90.2% of the amplitude without probe. For the Neuropixels MEA probe (C) the effect is in line with the Neuronexus probe, with a maximum difference of $41.07 \mu\text{V}$ (95.9% of the amplitude without probe) when the probe is closest and a minimum of $5.08 \mu\text{V}$, which is still 116.1% of the amplitude without probe, when the probe is located at the maximum distance. Note that the peak amplitudes on the microwire probe are smaller than the one measured on the MEAs at a similar distances. At the closest distance, for example, the Neuronexus MEA electrodes lie on the $y - z$ plane exactly at $7.5 \mu\text{m}$ from the somatic membrane. For the microwire, instead, $7.5 \mu\text{m}$ is the distance to the beginning of the cylindrical probe, whose tip extends in the x direction for $30 \mu\text{m}$. The simulated electric potential is the average of the electric potential computed on the microwire tip and it results in a much lower amplitude due to the fast decay of the extracellular potential with distance (see equation (13)).

In panel (D) of figure 5 we show the ratio between the peak with probe and without probe depending on the probe distance for the Neuronexus (red), Neuropixels (blue), and the microwire (grey) probes. The ratio for the microwire probe varies around 1 (average = 1.05), confirming that the *probe effect* can be neglected for microwire-like types of probe, due to their size and geometry. Instead, when a MEA probe is used, the average ratio is around 1.9 and its effect on the recordings cannot be neglected.

3.1.3. The probe effect is reduced when neuron and probe are not aligned. So far, we have shown results in which the neuron and the probe are perfectly aligned in the y direction, but the *probe effect* is likely to be affected by the neuron-probe

alignment, since the area of the MEA probe (we focus here on the Neuronexus and Neuropixels MEA probes as the effect using the microwire is negligible) *facing* the neuron changes depending on the lateral shift in the y direction and probe rotation.

To quantify the trend of the *probe effect* depending on the y shift, we ran simulations moving the probes at different y locations (10, 20, 30, 40, 50, 60, 80, and $100 \mu\text{m}$) and computed the ratios between the maximum peak with and without the MEA in the extracellular space. The simulations were run with *coarse 2* resolution and *boxsize 5* and the probe tip was at $40 \mu\text{m}$ from the center of the neuron. In figure 6(A) we show the peak ratios depending on lateral y shifts. The ratio appears to decrease almost linearly with the shifts, from a value of around 1.8–1.9 when the probe is centered (note that the peak ratio slightly varies depending on resolution and size, as covered in section 3.2) to a value of around 1.2 when the shift is $100 \mu\text{m}$ (the half width of the probe is $57 \mu\text{m}$ for Neuronexus and $35 \mu\text{m}$ for Neuropixels).

In order to evaluate the effect of rotating the probes, we ran simulations with the probe at $70 \mu\text{m}$ distance (to accommodate for different rotations), *coarse 2* resolution, *boxsize 4*, and rotations of $0, 30, 60, 90, 120, 150,$ and 180° . In figure 6(B) the peak ratios depending on the rotation angle are shown. For small or no rotations ($0, 30^\circ$) the value is around 1.7 (note that we always selected the electrode with the largest amplitude, which might not be the same electrode for all rotations). For a rotation of 90° the peak ratio is around 1 (the probe exposes its thinnest side to the neuron) and for further rotations the probe's shadowing effect makes the peak with the probe smaller (as observed in figure 4(C)), yielding peak ratio values below 1. These results demonstrate that the

Table 2. Solution variability depending on box (domain) size. The columns contain the maximum peak with the Neuronexus (MEA) probe, without the probe, the difference and ratio of the amplitudes with and without probe. The values are averaged over all resolutions.

Box size	V _{peak} with MEA (μV)	V _{peak} without MEA (μV)	Difference (μV)	Peak ratio
1	-40.12	-20.64	19.48	1.95
2	-41.46	-20.91	20.55	1.98
3	-41.91	-23.83	18.07	1.77
4	-43.10	-23.35	19.75	1.85
5	-43.09	-23.71	19.38	1.82

relative arrangement between the neuron and the probe play an important role in affecting the recorded signals.

3.2. EMI solution dependence on domain size and resolution

We generated meshes of four different resolutions and five different box sizes, as described in section 2.2, in order to investigate how the resolution and the domain size affect the finite element solutions. Since we are mainly interested in how the probe affects the extracellular potential and we showed that only for MEA probes this effect is large, we focus on the extracellular potential at the recording site with the maximum negative peak. We used the Neuronexus MEA probe for this analysis and the distance of the tip of the probe was $40\ \mu\text{m}$ (the recording sites plane is at $32.5\ \mu\text{m}$ from the somatic center). The recording site which experienced the largest potential deflection was at position $(32.5, 0, -13)\ \mu\text{m}$, i.e. the closest to the neuron soma in the axon direction. For a deeper examination of convergence of the EMI model refer to [6]. For resolutions *coarse 0* and *coarse 1* the box of size 4 and 5, and of size 5, respectively, were too large to be simulated.

In table 2 we show the values of the minimum EAP peak with and without the Neuronexus probe, their difference, and their ratio grouped by the domain (box) size and averaged over resolution. Despite some variability due to the numerical solution of the problem, there is a common trend in the peak values as the domain size increases: the minimum peaks tend to be larger in absolute values, both when the probe is in the extracellular space (from $-40.12\ \mu\text{V}$ for box size 1 to $-43.09\ \mu\text{V}$ for box size 5) and when it is not (from $-20.64\ \mu\text{V}$ for box size 1 to $-23.71\ \mu\text{V}$ for box size 5). This can be explained by the boundary conditions that we defined for the bounding box (equation (3)), which forces the electric potential at the boundaries to be 0. For this reason, a smaller domain size causes a steeper reduction of the extracellular potential from the neuron to the bounding box, making the peak amplitude, in absolute terms, smaller. The peak difference with and without the MEA probe appears to be relatively constant, but the peak ratio tends to slightly decrease with increasing domain size for the same reason expressed before (from 1.95 for box size 1 to 1.82 for box size 5). The solutions appear to be converging for box sizes 4 and 5, but the relative error (difference between box 1 and box 5 values divided by the value of box 5) is moderate (6.89% for the

Table 3. Solution variability depending on resolution (*Coarseness*). The columns contain the maximum peak with the Neuronexus (MEA) probe, without the probe, the difference and ratio of the amplitudes with and without probe. The values are computed with a box size 2.

Coarseness	V _{peak} with MEA (μV)	V _{peak} without MEA (μV)	Difference (μV)	Peak ratio
0	-41.74	-20.67	21.07	2.02
1	-40.74	-20.25	20.49	2.01
2	-41.26	-21.09	20.18	1.96
3	-42.11	-21.64	20.46	1.95

peak with probe, 12.95% for the peak without probe, and 4.14% for the peak ratio). Nevertheless, the 1.8–1.85 peak ratio values obtained with larger domain sizes should be a closer estimate of the true value.

Table 3 displays the same values of table 2, but with a fixed box size of 2 and varying resolution (*Coarseness*). The relative error (maximum difference across resolutions divided by the average values among resolutions) of the peak with the MEA is 3.3%, without the probe it is 6.65%, and for the peak ratio it is 3.53%.

Because the main purpose of this work was to qualitatively investigate the effect of various probe designs and the effect of distance, alignment, and rotation on the measurements, we used resolution *coarse 2* and box size 2, which represented an acceptable compromise between accuracy and simulation time. For investigating the effect of probe rotation and side shift we increased the box size to 4 and 5, respectively, to accommodate the position of the neural probe. Finally, in section 3.3 we increased the resolution to *coarse 0* and used box size 3 to obtain more accurate results for the comparison with the cable equation simulations.

3.3. Comparison with other approaches

After having investigated how an extracellular probe affects the amplitude of the recorded potentials and how this amplitude is modulated with distance, alignment, and rotation between the neuron and the probe, we now compare the EMI solution to other modeling approaches. We first analyze the differences between the EMI solution without the probe and the cable equation / current summation approach (CS) and between the EMI solution with the probe and the hybrid solution (HS). Then we focus on the HS, which combines a cable equation solution and an explicit model of the extracellular space, including the probe, in a FEM framework, and compare its solution to three correction strategies: the method of images (MoI), the scaled current summation (SCS), and the probe correction (PC).

In all the following simulations we used a mesh with *coarse 0* resolution and box size 3. The distance between the neuron soma center and the probe tip was $40\ \mu\text{m}$, resulting in recording sites on the $x = 32.5\ \mu\text{m}$ plane.

3.3.1. EMI, CS, and HS comparison. In order to compare the EMI simulations to conventional modeling, we built the

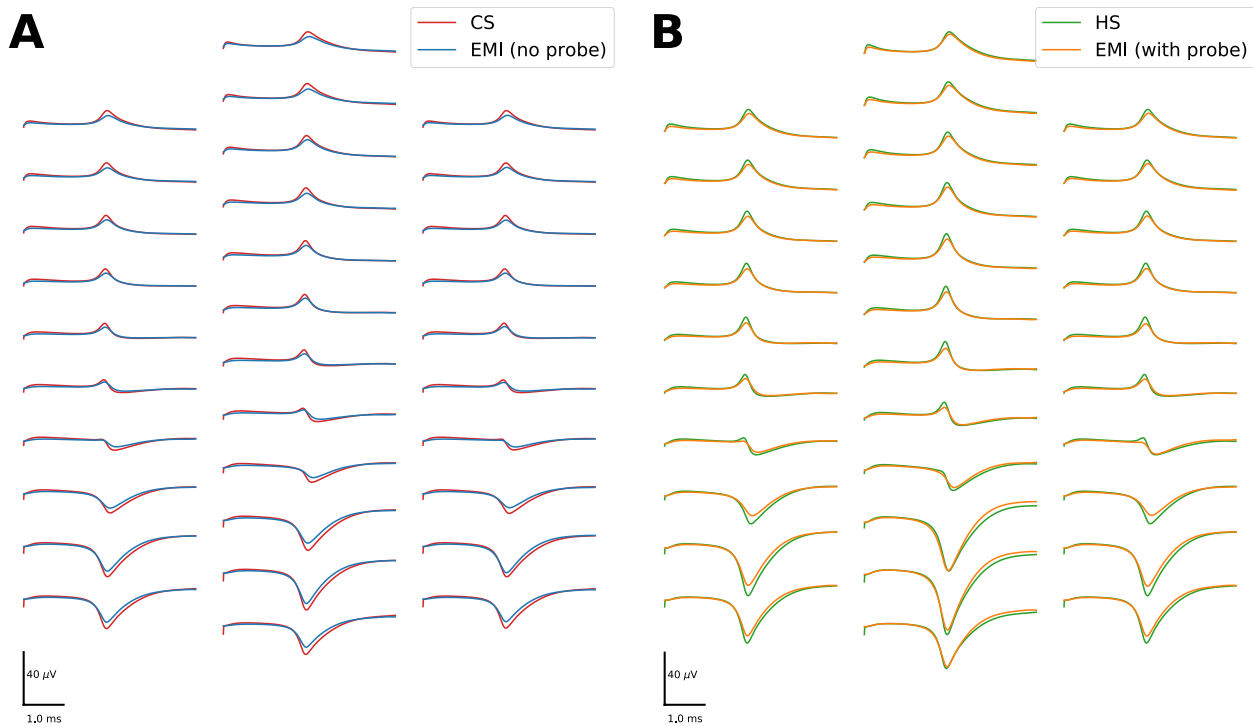


Figure 7. Comparison of the EAPs (A) between the current summation approach (CS, red) and the EMI model without probe (blue), displaying a peak amplitude difference of $4.91 \mu\text{V}$, and (B) between the hybrid solution (HS, green) and the EMI model with probe (orange), exhibiting a peak amplitude difference of $3.55 \mu\text{V}$.

same scenario shown in figure 2(B) (Neuronexus probe) using NEURON and LFPy, as described in section 2.4. As conventional modeling assumes an infinite and homogeneous medium, we compared the EAPs obtained by combining the cable equation solution (equation (12)) and the current summation formula (equation (13)) with the EMI simulations without the probe. The extracellular traces for the current summation approach (CS, red) and the EMI model (blue) are shown in figure 7(A). The EAPs almost overlap for every recording site, despite some differences in amplitude. On the electrode with the largest peak, the value for the EMI solution is $-23.03 \mu\text{V}$, while the value for the CS is $-27.95 \mu\text{V}$ (the difference is $4.91 \mu\text{V}$). This difference, which has been previously observed, is intrinsic to the EMI model [6], and can be due to self-ephaptic effects [6, 13–18]. Note also that the condition that forces the extracellular potential to zero at the boundary of the domain causes a steeper descent in the extracellular amplitudes, as discussed in section 3.2.

The hybrid solution (HS) uses currents computed with the cable equation and runs a FEM simulation of the extracellular space, including the probe. In figure 7(B) we show the extracellular potential of the EMI simulation with probe (orange) and the HS (green). Also in this case we observe that the EMI solution yields slightly smaller amplitudes with respect to the HS (EMI peak: $-42.6 \mu\text{V}$; HS peak $-46.15 \mu\text{V}$; difference: $3.55 \mu\text{V}$) and these differences can be once again traced back to underlying differences of the neural solver.

3.3.2. HS, MoI, SCS, and PC comparison. After having shown that there are intrinsic differences between the EMI model and solutions based on the cable equation (CS, HS), we

now compare two computationally less expensive strategies that could be used to account for the *probe effect* in modeling of extracellular potentials.

The MoI and SCS are attractive candidates due to their almost null computational cost, as they only multiply all values by a constant factor. The factor for infinite insulated planes, as described in section 2.4.1, is 2, but as shown in figures 5 and 6, for MEA probes it is somewhere between 0 and 2 depending on the neuron-probe lateral shift and rotation. In this scenario, the neuron is perfectly aligned with the probe and there is no rotation. The peak ratio for the SCS was computed by dividing the largest peaks of the HS and CS solutions and it was set to 1.65. In figure 8(A) the EAP from the HS (green), from the MoI (pink), and from the SCS with factor 1.65 (grey) are displayed. The MoI (pink) overshoots the estimation of the extracellular amplitudes (MoI peak: $-55.89 \mu\text{V}$; HS $-46.15 \mu\text{V}$; difference: $9.74 \mu\text{V}$). The SCS solution, expectedly, results in the same amplitude as the HS on the electrode with the largest peak, as the scaling factor was computed using the actual peak ratio between the HS and the CS solution. However, there are some discrepancies between HS and SCS. Figure 8(B) shows the distribution of peak ratios of all the 32 electrodes with respect to the HS peaks. The CS, MoI, and SCS solutions display a range of values in the peak ratios, showing that the amplitude modulation of the electrodes is not a constant value. This can be traced back to the fact that a lateral shift of the neuron reduces the peak ratio (figure 6(A)): electrodes on the side of the probe yield a lower effect than the ones at the center of the probe. Due to this variability, a correction strategy based on a constant scaling will not be able to accommodate for this effect.

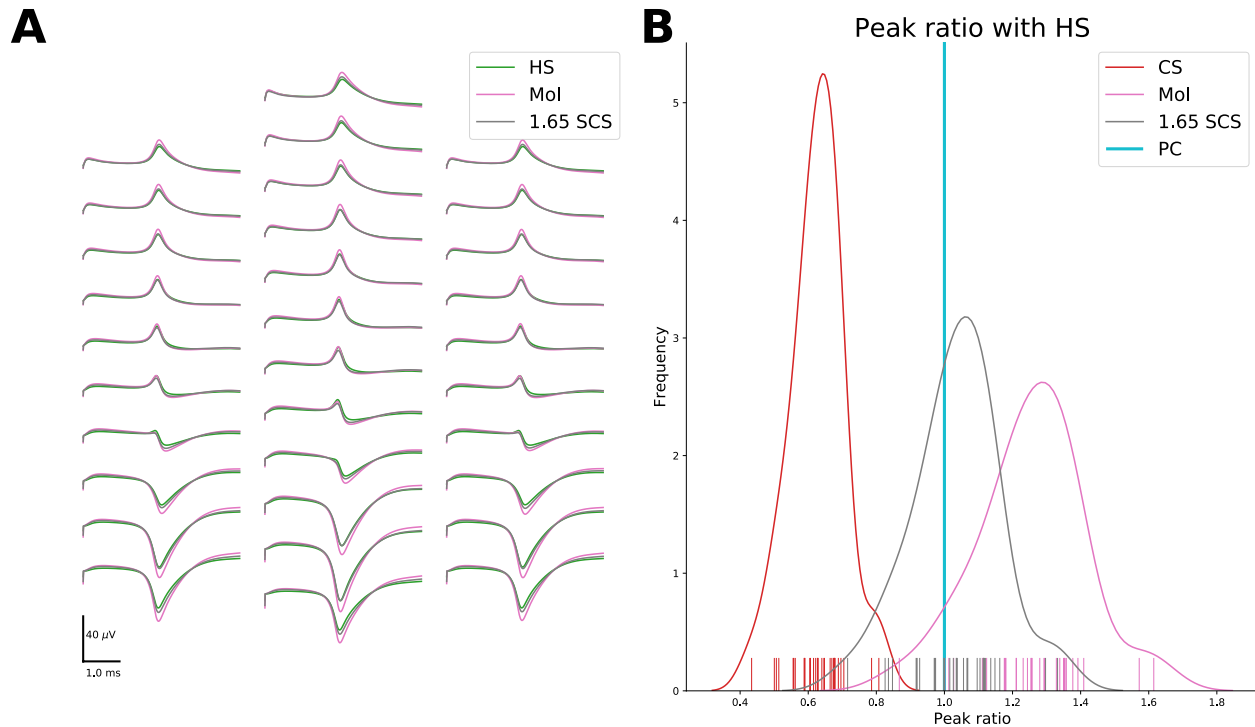


Figure 8. (A) EAPs of the Neuronexus probe as computed using the hybrid solution (HS, green), the Method of Images (MoI, pink) and the scaled current summation with factor 1.65 (1.65 SCS, grey). (B) Peak ratio distribution of the electrodes of the Neuronexus probe compared to the hybrid solution, from the current summation (CS, red), Method of Images (MoI, pink), the scaled current summation with factor 1.65 (1.65 SCS, grey), and the probe correction (PC, cyan) models. Note that the peak amplitudes computed from all the electrodes by the PC and HS approaches overlap perfectly, thus resulting in a single vertical line at peak ratio value 1.

The probe correction (PC) solution, based on the reciprocity principle (section 2.4.3), results in a solution perfectly coincident to the HS, at a much smaller computational cost (see table 5). In figure 8(B) the PC ratios are depicted as a vertical line at 1 because the peak amplitudes are exactly the same as the HS. The PC approach, in fact, pre-maps the effect of each electrode on the extracellular domain, effectively modeling in an efficient way the distribution of peak ratios observed when using the CS, MoI, and SCS methods.

In table 4 we summarize the comparison results, showing maximum, minimum, average peak ratios and the peak ratio distribution standard deviation for all the pairwise comparisons analyzed in this section.

3.4. CPU requirements

Whereas the EMI formulation represents a powerful and more detailed computational framework for neurophysiology simulations, it is associated with a much larger computational load. The simulations were performed on an Intel(R) Xeon(R) CPU E5-2623 v4 @ 2.60 GHz machine with 16 cores and 377 GB RAM running Ubuntu 16.04.3 LTS.

Table 5 contains the coarseness, domain size, number of tetrahedral cells, number of mesh vertices, total number of triangular cells (facets), facets on the surface of the neuron, the system size for the FEM problem, and the time in second (CPU time) to compute the solution for meshes without the probe in the extracellular domain. We show the results without probes in the extracellular domain, as they are computationally

Table 4. Summary of comparison results showing, for each comparison, the maximum, minimum, and average peak ratio, as well as the standard deviation of the peak ratio (PR) distribution. The peak ratios are the electrode-wise division between the peaks of the first and second models listed in the *Comparison* tab. *EMI (with)* and *EMI (no)* indicate the EMI solution with and without the probe in the extracellular space, respectively.

Comparison	Maximum PR	Minimum PR	Average PR	PR standard deviation
EMI (with)	2.16	1.4	1.81	0.19
EMI (no)				
CS—EMI (no)	1.6	1.16	1.39	0.1
HS—EMI (with)	1.49	1.01	1.25	0.11
CS—HS	0.81	0.43	0.63	0.08
MoI—HS	1.61	0.87	1.25	0.15
1.65 SCS—HS	1.33	0.72	1.03	0.13
PC—HS	1	1	1	0

more intense due to the fact that the volume inside the probe is not meshed (although the resolution on the probe surface is finer, the resulting system size without the probe is larger than with the probe). The CPU requirements and the time needed to run the simulation strongly depend on the resolution of the mesh: the problem with coarseness 3 and box size 3 takes around 1 h and 20 min (system size = 745 789), while for the same box size and coarseness 0, the time required is around

Table 5. Model type, FEM system size, resolution (*Coarseness*), box size, mesh parameters (number of cells, number of facets, number of neuron facets, and vertices), and CPU time to run the simulations. Note that for *coarse 2* and *coarse 3* the resolution of the neuron ($r_n = 4 \mu\text{m}$) is the same.

Model	System size	Coarse	Box size	Mesh Cells	Total facets	Neuron facets	Vertices	T (s)
EMI	337515	3	1	66171	135672	2552	12400	1414.24
EMI	516079	3	2	101443	207318	2552	18628	2813.22
EMI	562137	2	1	110363	225887	2480	20420	2589.83
EMI	745789	3	3	146905	299442	2552	26540	4569.11
EMI	835365	2	2	164331	335517	2480	29940	4753.39
EMI	1204001	2	3	237259	483371	2480	42666	10797.78
EMI	1225082	1	1	241402	491840	3888	43373	9593.98
EMI	1254096	3	4	247514	503291	2552	44013	10756.46
EMI	1881777	1	2	371471	755153	3888	65867	18880.78
EMI	1983058	3	5	391986	795536	2552	68875	23756.09
EMI	2110421	2	4	416949	846736	2480	73535	21582.90
EMI	2532813	0	1	501235	1015789	8376	87535	27676.91
EMI	2728288	1	3	539518	1094385	3888	94417	45430.64
EMI	3486058	2	5	689996	1398031	2480	119968	53132.75
EMI	3810512	0	2	755076	1527718	8376	130389	52495.76
EMI	4802239	1	4	951245	1925497	3888	164359	68474.42
EMI	5271370	0	3	1045440	2112965	8376	179195	82601.74
HS	403085	0	3	2299046	4665105	—	403085	3572.91
PC (map)	403085	0	3	2299046	4665105	—	403085	2015.02
PC (load)	403085	0	3	2299046	4665105	—	403085	409.91
PC (run)	403085	0	3	2299046	4665105	—	403085	3.51

22 h (system size = 5 271 370). The domain size also strongly affects the mesh size and computation time. For example, for the *coarse 2* resolution, with respect to *box 1*, *box 2* is 1.83 \times slower, *box 3* 4.16 \times , *box 4* 8.33 \times , *box 5* 20.51 \times .

The last four rows show the CPU requirements for the HS and the different steps of the PC solution. These simulations, despite having the same resolution and box size as the most intense EMI simulation (*coarse 0* and box size 3), result in a much smaller system size, as they solve for the extracellular potential only (EMI also solves for intracellular potentials and currents in the entire domain). To perform a fair comparison with the EMI model, the computations were done in serial. Parallel solvers would likely speed up the HS and PC solutions and could be easily implemented. Simulating 5 ms using the HS takes about 1 h, compared to the 22 h of the EMI solution. The PC performance is divided in three steps. *PC (map)* refers to the computation of the 32 FEM solutions (one for each Neuronexus electrode), and it takes slightly more than 30 min. Once the pre-map is computed it can be used for any neural model. Loading the FEM solutions in memory (*PC (load)*) requires around 7 min and once loaded, it takes a few seconds (3.51 s) to compute the extracellular potential. While the HS and EMI solutions computation time increases with the duration of the simulation linearly, as they iteratively solve each timestep, the PC solution multiplies each transmembrane current timeseries for a pre-defined mapping. When we ran a 500 ms NEURON simulation and then computed the extracellular potentials with the PC method the *PC (run)* step took only 5.38 s.

4. Discussion

In this article, we have used a detailed modeling framework—the extracellular-membrane-intracellular (EMI) model [6, 20]—to evaluate the effect of placing an extracellular recording device (neural probe) on the measured signals. We used meshes representing a simplified neuron and two different kind of probes: a microwire (a cylindrical probe with diameter of 30 μm) and multi-electrode arrays (MEAs), modeling a Neuronexus commercially available silicon probe and the Neuropixels probe [36]. We quantified the *probe effect* by simulating the domain with and without the probe in the extracellular domain and we showed that the effect is substantial for the MEA probes (figures 3(B) and (C)), while it is negligible for microwires (figure 3(A)). The amplitude of the largest peak using the MEA probes is almost twice as large (~ 1.9 times) compared to the case with no probe, and this factor is relatively independent of the probe distance (figure 5(D)), but it is reduced when the neuron and the probe are shifted laterally (figure 6(A)) or when the probe is rotated (figure 6(B)). Moreover, we discussed the effect of varying the mesh resolution and of the size of the computational domain. We also compared our finite element solutions to solutions obtained by solving the conventional cable equation, and found that the latter gave result very similar to the finite element solution when the probe was removed from the extracellular space (figure 7(A)). Therefore, we suggest that the *probe effect* can be a key element in modeling experimental data obtained with MEA probes. However, clearly further analysis is needed to

clarify this matter. At present the computational cost of the EMI model prevents simulations of neurons represented using realistic geometries. Thus, in an effort to offer less computationally expensive solutions to include the *probe effect* in simulations, we investigated various correction methods resulting in more accurate predictions and we proposed the probe correction method, which allows to obtain accurate solutions with reasonable computational cost and resources.

4.1. Comparison with previous work

In this work we used a finite element approach [20] to simulate the dynamics of a simplified neuron and to compute extracellular potentials using the EMI model. The use of FEM modeling for neural simulations has been performed before [19, 29, 30, 47, 48], but mainly as an advanced tool to study neural dynamics and ephaptic effects. In Moffit *et al* [47], the authors simulated, using the cable equation approach, a neuron at 65 μm from a shank microelectrode with a single recording site, and then used the currents in a finite element implementation of the extracellular domain, including the shank microelectrode. They found that the amplitude of the recorded potential with the shank was 77-100% larger than the analytical solution, but the spike shape was similar to the analytical solution (equation (13)), in accordance with our results (figures 7(A) and (B)). The effects using MEA probes and varying distances, lateral shifts, and probe rotations were not investigated. In Ness *et al* [25], an analytical framework for *in vitro* planar MEA using the method of images [24] was developed. A detailed neural model was simulated using the cable equation and transmembrane currents were used as forcing functions for a finite element simulation to validate the analytical solutions. In the *in vitro* case, in which the MEA is assumed to be an infinite insulating plane, the authors showed that the insulating MEA layer affects the amplitudes of the recorded potentials, effectively increasing it by a maximum factor of 2, which can be analytically predicted by the method of images (MoI).

In this study, we investigated how large the effect of commonly used *in vivo* probes is using the advanced EMI modeling framework. Our results are in line with these previous findings and we also show that the geometry, in terms of size and alignment of the probe, plays a very important role. We show that large silicon probes can be almost regarded as insulated planes when the neuron is aligned to them (potential increased by factor ~ 1.9) for large ranges of distances (figure 5(D)). An interesting effect following the reduction of the amplitude factor with lateral shifts (figure 6(A)) is that neurons not aligned with the probe will be recorded with a lower signal-to-noise ratio (SNR) due to the smaller amplitude increase, assuming that other sources of noise are invariant with respect to the probe location (such as electronic noise and biological noise from far neurons). This might bias neural recordings towards identifying neurons that are closer to the center of the probe, rather than the ones lying at the probes' sides. However, this conclusion is speculative and might be affected by other factors, such as the distribution of neurons

around the probe and their morphology (which contributes to the EAP). Therefore, ground truth information about the position of the recorded neurons and their reconstructed morphologies are needed for a quantitative evaluation of this phenomenon.

4.2. Limitations and extensions

4.2.1. Mesh improvements. The EMI model is, in principle, able to accurately represent the neuron and the neural probe. However, the accuracy of the model comes at the cost of computational resources. In order to be able to run simulations in a reasonable amount of time, the geometry of the neuron needed to be simplified considerably. First, we used a simple neuron in terms of a ball-and-stick with axon. This model is able to describe certain aspects of the neuronal dynamic [35], but it clearly cannot reach a level of detail of some more realistic morphologies, such as the reconstructed models made available by various initiatives [1–5]. We quantified the amplitude shift due to the probe in the extracellular domain (~ 1.9 on average for the MEA probes when neuron and probe are aligned), but this factor most likely also depend on the specific cell morphology that we used, and not only on the probe design and geometry. Therefore, we aim at extending the framework [49] for generating finite element meshes from publicly available realistic morphologies [5], allowing us to explore the *probe effect* for more complex morphologies.

Furthermore, we assumed *ideal* recording sites with an infinite input impedance which does not allow any current to flow in. In reality, recording electrodes have a high, but not infinite impedance that could be modeled by considering electrodes as an additional domain with very low conductance, even if it has been shown that for normal electrodes' impedance the effect of conductive and equipotential recording sites is negligible [32].

4.2.2. Computational costs. In section 3.4 we showed that the EMI model is *much more* computationally demanding than conventional modeling using cable and volume conduction theory. For the simplest simulation performed in this study (*coarse 3* and *box size 1*), a system with 337 515 unknowns was solved in about 40 min. The NEURON simulations described in section 2.4 took ~ 0.59 s to run, about 2400 times faster than the simplest EMI simulation performed here. However, because of our implementation and solution strategy for FEM, this factor should be considered as a rather pessimistic upper bound. In particular, the employed version of FEniCS (2017.2.0) does not allow for finite element spaces with components discretized on meshes with different topology. For example, the extra/intra-cellular potentials are defined on the entire Ω rather than Ω_e and Ω_i only, while the domain for the transmembrane potential v is Γ , but the space for v is setup on *all* facets of the mesh. For simplicity of implementation, the v unknowns on facets outside of Γ are forced to be zero by additional constraints and are not removed from the linear system. The LU solver thus solves also for the unphysical/extra unknowns and the memory footprint and solution times

are naturally higher. The number of unphysical unknowns can be seen in table 5 as a difference between total number of facets in the mesh and the number of facets on the surface of the neuron. For example, in the largest system considered here, avoiding the unphysical unknowns would reduce the system size by about 2 million.

In addition to assembling the linear system with only the physical unknowns, a potential speed up could be achieved by employing iterative solvers with suitable preconditioners. That is, fast PDE solvers for diffusion equations typically use around 1s per million degrees of freedom. As we here employ a H(div) formulation, we expect the solution to be computed in around 5 s per million degrees with multilevel methods. As shown in table 5, 500 timesteps of solving systems with around one million degrees of freedom takes 82 600 s, which means 165 s per time steps. Hence, we may expect to speed up the solving procedure by around a factor 30 with better solvers. If further speed-up is required then finite element based reduced basis function method provides an attractive approach that should be addressed in future research.

4.2.3. Finite element methods are not alternatives to the conventional cable equation. The EMI framework, due to its computational requirements, is presently not an alternative to conventional modeling involving the cable equation (equation (12)) and the current summation formula (equation (13)). However, for specific applications, it can provide interesting insights. The hybrid solution combines the cable equation solution to finite element modeling, in practice solving the FEM problem only for the extracellular space and using the transmembrane currents computed by the cable equation as forcing functions [21–23, 25, 47]. However, the HS is also computationally expensive and it increases in complexity with longer simulation durations. Similar considerations can be made if Boundary Element Methods (BEM) [50] are employed instead of FEM ones, even though they are less computationally intense than the current FEM formulation. One possible drawback of BEM solvers is that they could not accommodate for anisotropic conductivity, while FEM solvers could in principle solve meshes with non-homogeneous conductivity between surfaces [51].

Another much faster option could be using approaches based constant scaling, such as MoI and SCS. However, even correcting with a right factor smaller than 2, these methods cannot account for the variability of peak ratios among the electrodes (figure 8(B)). Therefore, we suggested here the probe correction (PC) method, which combines a one-time finite element simulation to model how each electrode of a specific probe affects the extracellular domain, and then uses the reciprocity principle to compute the potential on the recording sites arising from transmembrane currents. We showed that this method is able to reach the HS accuracy at a much smaller computational time (table 5), which is also not strongly dependent on the simulation duration. Moreover, the time required to compute the probe specific mapping (*PC (map)*) and loading the FEM solutions in memory (*PC (load)*) could be further reduced by decreasing the mesh resolution.

This possibility should be further investigated with a convergence analysis, similar to section 3.2 for the EMI model.

4.3. Significance of the probe effect

The effect of the recording device has not been fully taken into consideration in mathematical models of the extracellular field surrounding neurons. The *probe effect* needs to be considered when modeling silicon MEA, whose sizes are significantly larger than the recorded neurons. The assumption of an infinite and homogeneous medium is in fact largely violated when such *bulky* probes are in the extracellular space in the proximity of the cells. Although the tissue can be regarded as purely conductive and with a constant conductivity [52], these probes represent clear discontinuities in the extracellular conductivity, which strongly affect the measured potential due to their insulating properties. While the *probe effect* is large for MEAs, we found that it was negligible for microwire-type of probes, mainly for two reasons: first, the microwire is thinner and overall smaller than the MEA; second, the electric potential is sampled at the tip of the probe and in the entire semi-space below the microwire currents are free to flow without any obstacle.

When dealing with silicon MEAs, though, this effect could be crucial for certain applications that require to realistically describe recordings. For example, Gold *et al* [26] used, in simulation, extracellular action potentials (EAP) to constrain conductances of neuronal models. Clearly, neglecting the *probe effect* would result in an incorrect parameterization of the models in this case.

Another example in which including this effect could be beneficial is when EAP are used to localize the somata position with respect to the probe. This is traditionally done by solving the *inverse problem*: a simple model, such as a monopolar current source [53–55], a dipolar-current source [53, 56, 57], line-source models [58, 59], or a ball-and-stick model [60], is moved around the extracellular space to minimize the error between the recorded potential and the one generated by the model. Ignoring the probe might result in larger localization errors.

Recently, we used simulated EAP on MEA as *ground truth* data, from which features were extracted to train machine-learning methods to localize neurons [27, 28] and recognize their cell type from EAPs [28]. When training such machine-learning models on simulated data and applying them to experimental data, neglecting the *probe effect* could confound the trained model and yield prediction errors.

Moreover, explaining experimental recordings on MEA without considering the probe might cause discrepancies between the modeling and experimental results hard to reconcile. On the other hand, in order to fully explain and validate our findings, an experiment with accurate co-location of extracellular recordings and cell position (and ideally morphology) is required. For example, an experimental setup in which a planar MEA is combined with two-photon calcium imaging [61] could provide an accurate estimate of the relative position between the neurons and the MEA.

In conclusion, we presented numerical evidence that suggests that the *probe effect*, especially when using multi-electrode silicon probes, affects the way we model extracellular neural activity and interpret experimental data and cannot be neglected for specific applications.

Acknowledgments

APB and KHJ are part of the Simula-UCSD-University of Oslo Research and PhD training (SUURPh) program, an international collaboration in computational biology and medicine funded by the Norwegian Ministry of Education and Research. TVN would like to acknowledge the European Union Horizon 2020 Research and Innovation Programme under Grant Agreement No. 720270 and 785907 (Human Brain Project (HBP) SGA1 and SGA2). PB would like to acknowledge the Defense Advanced Research Project Agency (DARPA), Contract No. N66001-17-C-4002. The views, opinions and/or findings expressed are those of the author and should not be interpreted as representing the official views or policy of the Department of Defense of the U S Government.


ORCID iDs

Alessio Paolo Buccino  <https://orcid.org/0000-0003-3661-527X>

Miroslav Kuchta  <https://orcid.org/0000-0002-3832-0988>

Karoline Horgmo Jæger  <https://orcid.org/0000-0003-4234-9094>

Torbjørn Vefferstad Ness  <https://orcid.org/0000-0001-9080-8502>

Pierre Berthet  <https://orcid.org/0000-0002-6878-6842>

Kent-Andre Mardal  <https://orcid.org/0000-0002-4946-1110>

Gert Cauwenberghs  <https://orcid.org/0000-0002-3166-5529>

Aslak Tveito  <https://orcid.org/0000-0003-2362-146X>

References

- [1] Ramaswamy S et al 2015 The neocortical microcircuit collaboration portal: a resource for rat somatosensory cortex *Front. Neural Circuits* **9** 44
- [2] Markram H et al 2015 Reconstruction and simulation of neocortical microcircuitry *Cell* **163** 456–92
- [3] Gouwens N W, Berg J, Feng D, Sorensen S A, Zeng H, Hawrylycz M J, Koch C and Arkhipov A 2018 Systematic generation of biophysically detailed models for diverse cortical neuron types *Nat. Commun.* **9** 710
- [4] Ascoli G A 2006 Mobilizing the base of neuroscience data: the case of neuronal morphologies *Nat. Rev. Neurosci.* **7** 318
- [5] Ascoli G A, Donohue D E and Halavi M 2007 Neuromorpho.org: a central resource for neuronal morphologies *J. Neurosci.* **27** 9247–51
- [6] Tveito A, Jæger K H, Lines G T, Paszkowski Ł, Sundnes J, Edwards A G, Mäki-Marttunen T, Haldnes G and Einevoll G T 2017 An evaluation of the accuracy of classical models for computing the membrane potential and extracellular potential for neurons *Front. Comput. Neurosci.* **11** 27
- [7] Holt G R and Koch C 1999 Electrical interactions via the extracellular potential near cell bodies *J. Comput. Neurosci.* **6** 169–84
- [8] Gold C, Henze D A, Koch C and Buzsáki G 2006 On the origin of the extracellular action potential waveform: a modeling study *J. Neurophysiol.* **95** 3113–28
- [9] Carnevale N T and Hines M L 2006 *The NEURON Book* (Cambridge: Cambridge University Press) (<https://doi.org/10.1017/CBO9780511541612>)
- [10] Hines M L, Davison A P and Muller E 2009 NEURON and Python *Front. Neuroinf.* **3** 1
- [11] Lindén H, Hagen E, Leski S, Norheim E S, Pettersen K H and Einevoll G T 2014 LFPy: a tool for biophysical simulation of extracellular potentials generated by detailed model neurons *Front. Neuroinf.* **7** 41
- [12] Hagen E, Næss S, Ness T V and Einevoll G T 2018 Multimodal modeling of neural network activity: computing LFP, ECoG, EEG and MEG signals with LFPy 2.0 *Front. Neuroinform.* **12** 92
- [13] Buzsáki G, Anastassiou C A and Koch C 2012 The origin of extracellular fields and currents—EEG, ECoG, LFP and spikes *Nat. Rev. Neurosci.* **13** 407–20
- [14] Bhalla U S 2012 Multi-compartmental models of neurons *Computational Systems Neurobiology* (Berlin: Springer) pp 193–225
- [15] Goldwyn J H and Rinzel J 2016 Neuronal coupling by endogenous electric fields: cable theory and applications to coincidence detector neurons in the auditory brain stem *J. Neurophysiol.* **115** 2033–51
- [16] Anastassiou C A, Perin R, Markram H and Koch C 2011 Ephaptic coupling of cortical neurons *Nat. Neurosci.* **14** 217
- [17] Anastassiou C A and Koch C 2015 Ephaptic coupling to endogenous electric field activity: why bother? *Curr. Opin. Neurobiol.* **31** 95–103
- [18] Bokil H, Laaris N, Blinder K, Ennis M and Keller A 2001 Ephaptic interactions in the mammalian olfactory system *J. Neurosci.* **21** 1–5
- [19] Agudelo-Toro A and Neef A 2013 Computationally efficient simulation of electrical activity at cell membranes interacting with self-generated and externally imposed electric fields *J. Neural Eng.* **10** 026019
- [20] Tveito A, Jæger K H, Kuchta M, Mardal K-A and Rognes M E 2017 A cell-based framework for numerical modeling of electrical conduction in cardiac tissue *Front. Phys.* **5** 48
- [21] Capogrosso M, Wenger N, Raspopovic S, Musienko P, Beauparlant J, Luciani L B, Courtine G and Micera S 2013 A computational model for epidural electrical stimulation of spinal sensorimotor circuits *J. Neurosci.* **33** 19326–40
- [22] Lubba C H, Le Guen Y, Jarvis S, Jones N S, Cork S C, Eftekhari A and Schultz S R 2018 PyPNS: Multiscale simulation of a peripheral nerve in python *Neuroinformatics* **1–19**
- [23] Lertmanorat Z and Durand D M 2004 A novel electrode array for diameter-dependent control of axonal excitability: a simulation study *IEEE Trans. Biomed. Eng.* **51** 1242–50
- [24] Jackson J D 1975 *Electrodynamics* (New York: Wiley)
- [25] Ness T V, Chintaluri C, Potworowski J, Łęski S, Głąbska H, Wójcik D K and Einevoll G T 2015 Modelling and analysis of electrical potentials recorded in microelectrode arrays (MEAs) *Neuroinformatics* **13** 403–26
- [26] Gold C, Henze D A and Koch C 2007 Using extracellular action potential recordings to constrain compartmental models *J. Comput. Neurosci.* **23** 39–58
- [27] Buccino A P, Ness T V, Einevoll G T, Cauwenberghs G and Häfziger P D 2017 Localizing neuronal somata from multi-electrode array *in vivo* recordings using deep learning *39th Annual Int. Conf. IEEE Eng. Med. Biol. Soc. (IEEE)* pp 974–7

- [28] Buccino A P, Kordovan M, Ness T V, Merkt B, Häfliger P D, Fyhn M, Cauwenberghs G, Rotter S and Einevoll G T 2018 Combining biophysical modeling and deep learning for multi-electrode array neuron localization and classification *J. Neurophysiol.* **120** 1212–32
- [29] Krassowska W and Neu J C 1994 Response of a single cell to an external electric field *Biophys. J.* **66** 1768–76
- [30] Ying W and Henriquez C S 2007 Hybrid finite element method for describing the electrical response of biological cells to applied fields *IEEE Trans. Biomed. Eng.* **54** 611–20
- [31] Henriquez F, Jerez-Hanckes C and Altermatt M F R 2013 Dynamic finite-element model of axon extracellular stimulation *6th Int. IEEE/EMBS Conf. on Neural Engineering (IEEE)* pp 589–92
- [32] Moulin C, Glière A, Barbier D, Joucla S, Yvert B, Mailley P and Guillemaud R 2008 A new 3d finite-element model based on thin-film approximation for microelectrode array recording of extracellular action potential *IEEE Trans. Biomed. Eng.* **55** 683–92
- [33] Geuzaine C and Remacle J-F 2009 Gmsh: a 3d finite element mesh generator with built-in pre-and post-processing facilities *Int. J. Numer. Methods Eng.* **79** 1309–31
- [34] Mainen Z F, Joerges J, Huguenard J R and Sejnowski T J 1995 A model of spike initiation in neocortical pyramidal neurons *Neuron* **15** 1427–39
- [35] Pettersen K H and Einevoll G T 2008 Amplitude variability and extracellular low-pass filtering of neuronal spikes *Biophys. J.* **94** 784–802
- [36] Jun J J et al 2017 Fully integrated silicon probes for high-density recording of neural activity *Nature* **551** 232
- [37] Hodgkin A L and Huxley A F 1952 A quantitative description of membrane current and its application to conduction and excitation in nerve *J. Physiol.* **117** 500–44
- [38] Rognes M E, Farrell P E, Funke S W, Hake J E and Maleckar M 2017 Cbcbeat: an adjoint-enabled framework for computational cardiac electrophysiology *J. Open Source Softw.* **2** 224
- [39] Logg A, Mardal K-A and Wells G 2012 *Automated Solution of Differential Equations by the Finite Element Method: the FEniCS Book* vol 84 (Berlin: Springer) (<https://doi.org/10.1007/978-3-642-23099-8>)
- [40] Raviart P-A and Thomas J 1977 Primal hybrid finite element methods for 2nd order elliptic equations *Math. Comput.* **31** 391–413
- [41] Amestoy P R, Duff I S, Koster J and L'Excellent J-Y 2001 A fully asynchronous multifrontal solver using distributed dynamic scheduling *SIAM J. Matrix Anal. Appl.* **23** 15–41
- [42] Balay S et al 2018 PETSc Web page (www.mcs.anl.gov/petsc)
- [43] Sterratt D, Graham B, Gillies A and Willshaw D 2011 *Principles of Computational Modelling in Neuroscience* (Cambridge: Cambridge University Press) (<https://doi.org/10.1017/CBO9780511975899>)
- [44] Ermentrout G B and Terman D H 2010 *Mathematical Foundations of Neuroscience* vol 35 (Berlin: Springer) (<https://doi.org/10.1007/978-0-387-87708-2>)
- [45] Scott A 2002 *Neuroscience: a Mathematical Primer* (Berlin: Springer) (<https://doi.org/10.1007/b98897>)
- [46] Panofsky W K and Phillips M 2005 *Classical Electricity and Magnetism* (Mineola, NY: Dover)
- [47] Moffitt M A and McIntyre C C 2005 Model-based analysis of cortical recording with silicon microelectrodes *Clin. Neurophysiol.* **116** 2240–50
- [48] Lempka S F and McIntyre C C 2013 Theoretical analysis of the local field potential in deep brain stimulation applications *PloS One* **8** e59839
- [49] Mörschel K, Breit M and Queisser G 2017 Generating neuron geometries for detailed three-dimensional simulations using anamorph *Neuroinformatics* **15** 247–69
- [50] Gramfort A, Papadopoulo T, Olivi E and Clerc M 2010 OpenMEEG: opensource software for quasistatic bioelectromagnetics *Biomed. Eng. online* **9** 45
- [51] Clerc M, Dervieux A, Faugeras O, Keriven R, Kybic J and Papadopoulo T 2002 Comparison of BEM and FEM methods for the E/MEG problem *Proc. of BIOMAG Conf.* (Citeseer)
- [52] Goto T, Hatanaka R, Ogawa T, Sumiyoshi A, Riera J and Kawashima R 2010 An evaluation of the conductivity profile in the somatosensory barrel cortex of wistar rats *J. Neurophysiol.* **104** 3388–412
- [53] Blanche T J, Spacek M A, Hetke J F and Swindale N V 2005 Polytrodes: high-density silicon electrode arrays for large-scale multiunit recording *J. Neurophysiol.* **93** 2987–3000
- [54] Chelaru M I and Jog M S 2005 Spike source localization with tetrodes *J. Neurosci. Methods* **142** 305–15
- [55] Kubo T, Katayama N, Karashima A and Nakao M 2008 The 3d position estimation of neurons in the hippocampus based on the multi-site multi-unit recordings with silicon tetraodes *30th Annual Int. Conf. IEEE Eng. Med. Biol. Soc. (IEEE)* pp 5021–4
- [56] Mechler F, Victor J D, Ohiorhenuan I, Schmid A M and Hu Q 2011 Three-dimensional localization of neurons in cortical tetraode recordings *J. Neurophysiol.* **106** 828–48
- [57] Mechler F and Victor J D 2012 Dipole characterization of single neurons from their extracellular action potentials *J. Comput. Neurosci.* **32** 73–100
- [58] Somogyvári Z, Zalányi L, Ulbert I and Érdi P 2005 Model-based source localization of extracellular action potentials *J. Neurosci. Methods* **147** 126–37
- [59] Somogyvári Z, Cserpán D, Ulbert I and Érdi P 2012 Localization of single-cell current sources based on extracellular potential patterns: the spike CSD method *Eur. J. Neurosci.* **36** 3299–313
- [60] Ruz I D and Schultz S R 2014 Localising and classifying neurons from high density MEA recordings *J. Neurosci. Methods* **233** 115–28
- [61] Shew W L, Bellay T and Plenz D 2010 Simultaneous multi-electrode array recording and two-photon calcium imaging of neural activity *J. Neurosci. Methods* **192** 75–82